

# The contribution of dilatational motion to energy flux in homogeneous compressible turbulence

By Chensheng Luo<sup>1,2,3</sup>, Le Fang<sup>3,2</sup>, Jian Fang<sup>4</sup>, Haitao Xu<sup>5</sup>, Alain Pumir<sup>6</sup> and Ping-Fan Yang<sup>1,5,7</sup>†

<sup>1</sup> School of Aeronautics and Institute of Extreme Mechanics, Northwestern Polytechnical University, Xi'an, 710072, PR China

<sup>2</sup> Research Institute of Aero-Engine, Beihang University, Beijing 100191, PR China

<sup>3</sup> Laboratory of Complex System, Ecole Centrale de Pékin/School of General Engineering, Beihang University, Beijing 100191, PR China

<sup>4</sup> Scientific Computing Department, STFC Daresbury Laboratory, Warrington WA4 4AD, UK

<sup>5</sup> Center for Combustion Energy and School of Aerospace Engineering Tsinghua University, Beijing, 100084, PR China

<sup>6</sup> Laboratoire de Physique, Ecole Normale Supérieure de Lyon, CNRS Université de Lyon, Lyon, F-69007 France

<sup>7</sup> National Key Laboratory of Aircraft Configuration Design, Xi'an 710072, China

(Received 9 October 2024)

We analyze the energy flux in compressible turbulence by generalizing the exact decomposition recently proposed by Johnson (Phys. Rev. Lett., vol. 124, 2020. 104501) to study incompressible turbulent flows. This allows us to characterize the effect of dilatational motion on the inter-scale energy transfer in three-dimensional compressible turbulence. Our analysis reveals that the contribution of dilatational motion to energy transfer is due to three different physical mechanisms: the interaction between dilatation and strain, between dilatation and vorticity, and the self-interaction of dilatational motion across scales. By analyzing numerical simulations of flows at moderate turbulent Mach numbers ( $Ma_t \lesssim 0.3$ ), we validate our theoretical derivations and provide a quantitative description of the role of dilatational motion in energy transfer. In particular, we determine the scaling dependence of the dilatational contributions on the turbulent Mach number. Moreover, our findings reveal that the eddy-viscosity assumption often used in large-eddy simulations, in the spirit of the approach used for incompressible flows, effectively neglects the interaction between solenoidal-dilatational energy transfer and overestimate dilatational effects.

## 1. Introduction

Fluid turbulence is characterized by a wide range of spatial scales, and understanding how energy is distributed and transferred across scales is a fundamental problem. In three-dimensional (3D) incompressible turbulence, energy undergoes a cascade from the largest scales of the system, where energy is injected, to the smallest scales, where it is dissipated (Richardson 1922; Monin & Yaglom 1975; Tennekes & Lumley 1972; Frisch 1995; Pope 2000; Davidson 2015). One of the clearest signatures of the cascade comes

† Email address for correspondence: yangpingfan@nwpu.edu.cn

from the third-order velocity structure function, which satisfies the Kármán-Howarth equation (Von Kármán & Howarth 1938). This leads to the celebrated four-fifths law for the third-order structure function (Kolmogorov 1941*a,b*), which indicates energy transfer from large to small scale in the inertial range of turbulence. An alternative approach to quantify energy transfer consists in studying the problem in Fourier space, which leads to the Kármán-Lin equation for the energy spectrum (Lin 1947; Von Kármán & Lin 1951), or the subgrid-scale (SGS) stress (Eyink 2006; Ballouz & Ouellette 2018, 2020; Dong *et al.* 2020) in the filtered energy equation within the Large Eddy Simulation (LES) formalism (Germano 1992; Meneveau & Katz 2000; Moser *et al.* 2021; Sagaut 2006). Recent attempts have been made to relate the descriptions in Fourier and in real space (Goto *et al.* 2017; McKeown *et al.* 2023).

Energy transfer is of broader interest than just for incompressible turbulence. Here, we focus on compressible flows, which are of interest not only for fundamental reasons but also for applications to supersonic flows (Kovaszny 1953; Spina *et al.* 1994; Modesti *et al.* 2022), ramjets (Waltrup 1987; Billig 1988; Curran *et al.* 1996), volcanic eruptions (Ogden *et al.* 2008) and interstellar turbulences (Elmegreen & Scalo 2004; Scalo & Elmegreen 2004; Chernyshov *et al.* 2010; Ferrand *et al.* 2020). Numerous studies have investigated the statistics and scaling in compressible turbulence (Samtaney *et al.* 2001; Pirozzoli & Grasso 2004; Wang *et al.* 2012*a,b*, 2017; Jagannathan & Donzis 2016; Donzis & John 2020), especially the inter-scale energy transfer (Bataille & Zhou 1999; Aluie 2011; Aluie *et al.* 2012; Aluie 2013; Eyink & Drivas 2018; Schmidt & Grete 2019). Conceptually, one may use approaches in terms of structure function (Falkovich *et al.* 2010; Galtier & Banerjee 2011; Wagner *et al.* 2012; Kritsuk *et al.* 2013; Banerjee & Galtier 2014; Lai *et al.* 2018; Lindborg 2019; Hellinger *et al.* 2021*a,b*), or focus on the spectral approach (Kida & Orszag 1992; Miura & Kida 1995).

In general, the introduction of compressibility adds considerable complexity compared to the incompressible case, and it is challenging to extend known theoretical results to compressible turbulence. Difficulties arise as a consequence of varying density, and generally because the velocity gradient tensor is not divergence-free. Generalizations of the Kármán-Howarth equation to compressible flows require density-weighted velocity and velocity structure function (Kida & Orszag 1992; Falkovich *et al.* 2010; Galtier & Banerjee 2011; Wagner *et al.* 2012; Lai *et al.* 2018; Hellinger *et al.* 2021*b*), which considerably complicates the mathematical expressions and blurs the physical interpretations of the various terms in the generalized Kármán-Howarth equation. Additionally, the presence of non-zero divergence in the velocity gradient prevents us from obtaining a straightforward relation akin to the four-fifths law observed in incompressible turbulence. These challenges hinder our understanding of how density fluctuations and dilatational motion impact energy transfer in compressible turbulence. Similar difficulties arise when attempting a description in Fourier space. To fully utilize the theoretical findings from incompressible turbulence, a common approach is to decompose the compressible velocity field into solenoidal (divergence-free) and dilatational (compressive) components using Helmholtz decomposition. However, the fluctuation of density complicates this decomposition. Some studies (Fauchet 1998; Bataille & Zhou 1999; Falkovich & Kritsuk 2017; Sagaut & Cambon 2018) apply the Helmholtz decomposition directly to the velocity field  $\mathbf{u}$ , resulting in a solenoidal mode with zero divergence, but excluding density variations from the kinetic energy spectrum. Other studies (Kida & Orszag 1992; Miura & Kida 1995; Wang *et al.* 2013) decompose the density-weighted velocity field  $\mathbf{w} = \sqrt{\rho}\mathbf{u}$ , which takes into account density fluctuations and ensures positive-definiteness, but yields a solenoidal velocity field that is not strictly divergence-free, complicating the physical interpretation of the density-weighted velocity  $\mathbf{w}$ .

In this work, we address these technical challenges by applying a filtering approach and extending the formalism recently proposed by Johnson (2020, 2021) to compressible turbulence, and unveil the physical mechanism associated with dilatational motion. Johnson (2020) previously showed that the SGS stress can be expressed as an integral of the filtered velocity gradient across all sub-filter scales. This approach identifies three mechanisms contributing to energy flux: strain-self amplification, vortex stretching, and mixed strain-vorticity interaction. By conducting Direct Numerical Simulations (DNSs), Johnson (2020) revealed that strain-self amplification dominates the energy cascade process. This formalism has also been extended to sheared, stably stratified turbulence (Zhang *et al.* 2022) and helical turbulence (Capocci *et al.* 2023). Here, we show that when applied to compressible turbulence, this approach helps identify how dilatational motion contributes to the energy flux.

In §2, we will first generalize the relation between SGS stress and filtered velocity gradient for incompressible turbulence with a Gaussian filter, introduced by Johnson (2020, 2021), to the case of compressible turbulence using the Favre filtering, and introduce new mechanisms associated with dilatational motion. Then, in §3 and §4, we will use DNS data to verify our theoretical derivation and analyze the dilatational contribution to energy transfer. Finally, in §5, we summarize the results of this work.

## 2. Relation between SGS stress and filtered velocity gradient in compressible turbulence

We first start from the subgrid-scale (SGS) stress term in compressible turbulence:

$$\tau_{ij}^\ell = \overline{\rho^\ell u_i u_j}^\ell - \overline{\rho^\ell \tilde{u}_i \tilde{u}_j}^\ell = \overline{\rho u_i u_j}^\ell - \frac{1}{\overline{\rho^\ell}} \overline{\rho u_i^\ell \rho u_j^\ell}, \quad (2.1)$$

where the symbol  $\overline{\cdot}^\ell$  and  $\tilde{\phi}^\ell = \overline{\rho \phi}^\ell / \overline{\rho}^\ell$  denote the spatial and Favre filtering at scale  $\ell$ , see, *e.g.*, Chai & Mahesh (2012) and Qi *et al.* (2022). If we choose the spatial filter to be Gaussian, then we have the following identity (Johnson 2020, 2021):

$$\frac{\partial \overline{\phi}^\ell}{\partial \ell^2} = \frac{1}{2} \nabla^2 \overline{\phi}^\ell. \quad (2.2)$$

To address the effect of density fluctuation, we need to evaluate derivatives related to Favre filtering. We first look at  $\frac{\partial \tilde{\phi}^\ell}{\partial \ell^2}$ :

$$\frac{\partial \tilde{\phi}^\ell}{\partial \ell^2} = \frac{\partial}{\partial \ell^2} \left( \frac{\overline{\rho \phi}^\ell}{\overline{\rho}^\ell} \right) = \frac{1}{2} \left[ \frac{1}{\overline{\rho}^\ell} \nabla^2 (\overline{\rho \phi}^\ell) - \frac{\overline{\rho \phi}^\ell}{(\overline{\rho}^\ell)^2} \nabla^2 (\overline{\rho}^\ell) \right]. \quad (2.3)$$

Next we consider  $\nabla^2 \tilde{\phi}^\ell$ :

$$\nabla^2 \tilde{\phi}^\ell = \nabla^2 \left( \frac{\overline{\rho \phi}^\ell}{\overline{\rho}^\ell} \right) = \frac{1}{\overline{\rho}^\ell} \nabla^2 (\overline{\rho \phi}^\ell) - \frac{2}{(\overline{\rho}^\ell)^2} \frac{\partial \overline{\rho}^\ell}{\partial x_k} \frac{\partial \overline{\rho \phi}^\ell}{\partial x_k} + \frac{2 \overline{\rho \phi}^\ell}{(\overline{\rho}^\ell)^3} \frac{\partial \overline{\rho}^\ell}{\partial x_k} \frac{\partial \overline{\rho}^\ell}{\partial x_k} - \frac{\overline{\rho \phi}^\ell}{(\overline{\rho}^\ell)^2} \nabla^2 (\overline{\rho}^\ell). \quad (2.4)$$

Subtracting one-half of Eq. (2.4) from Eq. (2.3) yields:

$$\frac{\partial \tilde{\phi}^\ell}{\partial \ell^2} - \frac{1}{2} \nabla^2 \tilde{\phi}^\ell = \frac{1}{(\overline{\rho}^\ell)^2} \frac{\partial \overline{\rho}^\ell}{\partial x_k} \frac{\partial \overline{\rho \phi}^\ell}{\partial x_k} - \frac{\overline{\rho \phi}^\ell}{(\overline{\rho}^\ell)^3} \frac{\partial \overline{\rho}^\ell}{\partial x_k} \frac{\partial \overline{\rho}^\ell}{\partial x_k} = \frac{1}{\overline{\rho}^\ell} \frac{\partial \overline{\rho}^\ell}{\partial x_k} \frac{\partial \tilde{\phi}^\ell}{\partial x_k}. \quad (2.5)$$

Now with the help of Eq. (2.5), we evaluate  $\frac{\partial \tau_{ij}^\ell}{\partial \ell^2}$ :

$$\begin{aligned} \frac{\partial \tau_{ij}^\ell}{\partial \ell^2} &= \frac{\partial \bar{\rho}^\ell}{\partial \ell^2} \widetilde{u_i u_j}^\ell + \bar{\rho}^\ell \frac{\partial \widetilde{u_i u_j}^\ell}{\partial \ell^2} - \frac{\partial \bar{\rho}^\ell}{\partial \ell^2} \widetilde{u_i}^\ell \widetilde{u_j}^\ell - \bar{\rho}^\ell \frac{\partial \widetilde{u_i}^\ell}{\partial \ell^2} \widetilde{u_j}^\ell - \bar{\rho}^\ell \widetilde{u_i}^\ell \frac{\partial \widetilde{u_j}^\ell}{\partial \ell^2} \\ &= \left[ \frac{1}{2} \nabla^2 (\bar{\rho}^\ell) \widetilde{u_i u_j}^\ell \right] + \left[ \frac{1}{2} \bar{\rho}^\ell \nabla^2 \widetilde{u_i u_j}^\ell + \frac{\partial \bar{\rho}^\ell}{\partial x_k} \frac{\partial \widetilde{u_i u_j}^\ell}{\partial x_k} \right] - \left[ \frac{1}{2} \nabla^2 (\bar{\rho}^\ell) \widetilde{u_i}^\ell \widetilde{u_j}^\ell \right] \\ &\quad - \left[ \frac{1}{2} \bar{\rho}^\ell \nabla^2 (\widetilde{u_i}^\ell) \widetilde{u_j}^\ell + \frac{\partial \bar{\rho}^\ell}{\partial x_k} \frac{\partial \widetilde{u_i}^\ell}{\partial x_k} \widetilde{u_j}^\ell \right] - \left[ \frac{1}{2} \bar{\rho}^\ell \nabla^2 (\widetilde{u_j}^\ell) \widetilde{u_i}^\ell + \frac{\partial \bar{\rho}^\ell}{\partial x_k} \frac{\partial \widetilde{u_j}^\ell}{\partial x_k} \widetilde{u_i}^\ell \right]. \end{aligned} \quad (2.6)$$

On the other hand, we also have:

$$\begin{aligned} \frac{1}{2} \nabla^2 \tau_{ij}^\ell &= \frac{1}{2} \frac{\partial}{\partial x_k} \left( \frac{\partial \bar{\rho}^\ell}{\partial x_k} \widetilde{u_i u_j}^\ell + \bar{\rho}^\ell \frac{\partial \widetilde{u_i u_j}^\ell}{\partial x_k} - \frac{\partial \bar{\rho}^\ell}{\partial x_k} \widetilde{u_i}^\ell \widetilde{u_j}^\ell - \bar{\rho}^\ell \frac{\partial \widetilde{u_i}^\ell}{\partial x_k} \widetilde{u_j}^\ell - \bar{\rho}^\ell \widetilde{u_i}^\ell \frac{\partial \widetilde{u_j}^\ell}{\partial x_k} \right) \\ &= \frac{1}{2} \nabla^2 (\bar{\rho}^\ell) \widetilde{u_i u_j}^\ell + \frac{1}{2} \bar{\rho}^\ell \nabla^2 \widetilde{u_i u_j}^\ell + \frac{\partial \bar{\rho}^\ell}{\partial x_k} \frac{\partial \widetilde{u_i u_j}^\ell}{\partial x_k} - \frac{1}{2} \nabla^2 (\bar{\rho}^\ell) \widetilde{u_i}^\ell \widetilde{u_j}^\ell - \frac{\partial \bar{\rho}^\ell}{\partial x_k} \frac{\partial \widetilde{u_i}^\ell}{\partial x_k} \widetilde{u_j}^\ell \\ &\quad - \frac{\partial \bar{\rho}^\ell}{\partial x_k} \frac{\partial \widetilde{u_j}^\ell}{\partial x_k} \widetilde{u_i}^\ell - \bar{\rho}^\ell \frac{\partial \widetilde{u_i}^\ell}{\partial x_k} \frac{\partial \widetilde{u_j}^\ell}{\partial x_k} - \frac{1}{2} \bar{\rho}^\ell \nabla^2 (\widetilde{u_i}^\ell) \widetilde{u_j}^\ell - \frac{1}{2} \bar{\rho}^\ell \nabla^2 (\widetilde{u_j}^\ell) \widetilde{u_i}^\ell. \end{aligned} \quad (2.7)$$

Subtracting Eq. (2.7) from Eq. (2.6) yields:

$$\frac{\partial \tau_{ij}^\ell}{\partial \ell^2} = \frac{1}{2} \nabla^2 \tau_{ij}^\ell + \bar{\rho}^\ell \frac{\partial \widetilde{u_i}^\ell}{\partial x_k} \frac{\partial \widetilde{u_j}^\ell}{\partial x_k}. \quad (2.8)$$

The solution of Eq. (2.8) is:

$$\begin{aligned} \tau_{ij}^\ell &= \int_0^{\ell^2} \frac{\overline{\bar{\rho}^{\sqrt{\alpha}} \frac{\partial \widetilde{u_i}^{\sqrt{\alpha}}}{\partial x_k} \frac{\partial \widetilde{u_j}^{\sqrt{\alpha}}}{\partial x_k}}^{\sqrt{\ell^2 - \alpha}}}{\bar{\rho}^{\sqrt{\alpha}} \widetilde{A}_{ik}^{\sqrt{\alpha}} \widetilde{A}_{jk}^{\sqrt{\alpha}}} d\alpha, \\ &= \int_0^{\ell^2} \frac{\overline{\bar{\rho}^{\sqrt{\alpha}} \widetilde{S}_{ik}^{\sqrt{\alpha}} \widetilde{S}_{jk}^{\sqrt{\alpha}}}}^{\sqrt{\ell^2 - \alpha}}}{\bar{\rho}^{\sqrt{\alpha}} \widetilde{A}_{ik}^{\sqrt{\alpha}} \widetilde{A}_{jk}^{\sqrt{\alpha}}} d\alpha, \end{aligned} \quad (2.9)$$

where  $\widetilde{A}_{ij}^\ell \equiv \partial \widetilde{u_i}^\ell / \partial x_j$  is the gradient of the Favre-filtered velocity, referred to in the following as filtered velocity gradient. Its divergence-free, symmetric and anti-symmetric parts are defined by:  $\widetilde{S}_{ij}^\ell = (\widetilde{A}_{ij}^\ell + \widetilde{A}_{ji}^\ell) / 2 - \widetilde{A}_{ll}^\ell \delta_{ij} / 3$  and  $\widetilde{W}_{ij}^\ell = (\widetilde{A}_{ij}^\ell - \widetilde{A}_{ji}^\ell) / 2$ , respectively. Note that Eq. (2.9) in our text and Eq. (10) in Johnson (2020) share a similar form, the differences being that a factor of density appears, and the substitution of standard filtering with Favre filtering for the filtered velocity gradient in the compressible case considered here.

The quantity  $\Pi^\ell \equiv \tau_{ij}^\ell \frac{\partial \widetilde{u_i}^\ell}{\partial x_j}$  represents the energy transfer across length scale  $\ell$ . By substituting the velocity gradient decomposition  $\widetilde{A}_{ij} = \widetilde{S}_{ij} + \widetilde{W}_{ij} + \widetilde{A}_{ll} \delta_{ij} / 3$  into Eq. (2.9), the inter-scale energy transfer term  $\Pi^\ell$  decomposes as follows:

$$\Pi^\ell = \underbrace{\Pi_{s1}^\ell + \Pi_{s2}^\ell + \Pi_{s3}^\ell}_{\Pi_s^\ell} + \underbrace{\Pi_{m1}^\ell + \Pi_{m2}^\ell + \Pi_{m3}^\ell}_{\Pi_m^\ell} + \Pi_d^\ell, \quad (2.10)$$

where,

$$\Pi_{s1}^\ell = \int_0^{\ell^2} d\alpha \bar{\rho}^{\sqrt{\alpha}} \widetilde{S}_{ik}^{\sqrt{\alpha}} \widetilde{S}_{jk}^{\sqrt{\alpha}} \widetilde{S}_{ij}^\ell, \quad (2.11a)$$

$$\Pi_{s2}^\ell = - \int_0^{\ell^2} d\alpha \overline{\rho^{\sqrt{\alpha}} \widetilde{W}_{ik}^{\sqrt{\alpha}} \widetilde{W}_{kj}^{\sqrt{\alpha}}}^{\sqrt{\ell^2-\alpha}} \widetilde{S}_{ij}^\ell, \quad (2.11b)$$

$$\Pi_{s3}^\ell = \int_0^{\ell^2} d\alpha \overline{\rho^{\sqrt{\alpha}} \left( \widetilde{S}_{kj}^{\sqrt{\alpha}} \widetilde{W}_{ik}^{\sqrt{\alpha}} - \widetilde{S}_{ik}^{\sqrt{\alpha}} \widetilde{W}_{kj}^{\sqrt{\alpha}} \right)}^{\sqrt{\ell^2-\alpha}} \widetilde{S}_{ij}^\ell, \quad (2.11c)$$

$$\Pi_{m1}^\ell = \frac{2}{3} \int_0^{\ell^2} d\alpha \overline{\rho^{\sqrt{\alpha}} \widetilde{A}_{ll}^{\sqrt{\alpha}} \widetilde{S}_{ij}^{\sqrt{\alpha}}}^{\sqrt{\ell^2-\alpha}} \widetilde{S}_{ij}^\ell, \quad (2.11d)$$

$$\Pi_{m2}^\ell = \frac{1}{3} \int_0^{\ell^2} d\alpha \overline{\rho^{\sqrt{\alpha}} \widetilde{S}_{ij}^{\sqrt{\alpha}} \widetilde{S}_{ij}^{\sqrt{\alpha}}}^{\sqrt{\ell^2-\alpha}} \widetilde{A}_{ll}^\ell, \quad (2.11e)$$

$$\Pi_{m3}^\ell = -\frac{1}{3} \int_0^{\ell^2} d\alpha \overline{\rho^{\sqrt{\alpha}} \widetilde{W}_{ij}^{\sqrt{\alpha}} \widetilde{W}_{ji}^{\sqrt{\alpha}}}^{\sqrt{\ell^2-\alpha}} \widetilde{A}_{ll}^\ell, \quad (2.11f)$$

$$\Pi_d^\ell = \frac{1}{9} \int_0^{\ell^2} d\alpha \overline{\rho^{\sqrt{\alpha}} \widetilde{A}_{ii}^{\sqrt{\alpha}} \widetilde{A}_{jj}^{\sqrt{\alpha}}}^{\sqrt{\ell^2-\alpha}} \widetilde{A}_{kk}^\ell. \quad (2.11g)$$

In Eq. (2.10), the inter-scale energy transfer is decomposed into three parts:  $\Pi_s^\ell$ , the energy transfer within the solenoidal mode;  $\Pi_m^\ell$ , the mixed energy transfer between the solenoidal and the dilatational modes; and  $\Pi_d^\ell$ , the energy transfer within the dilatational mode. More precisely, the solenoidal energy transfer has three contributions:  $\Pi_{s1}^\ell$ ,  $\Pi_{s2}^\ell$  and  $\Pi_{s3}^\ell$ , which represent the energy transfer due to the interaction of strain at scale  $\ell$  with strain (see Eq. (2.11a)), vorticity (see Eq. (2.11b)), and strain-vorticity correlations (see Eq. (2.11c)) at a scale smaller than or equal to  $\ell$ , respectively. These terms correspond to  $\Pi_S^\ell$ ,  $\Pi_\Omega^\ell$  and  $\Pi_c^\ell$  introduced in the incompressible case by Johnson (2020) and Yang *et al.* (2023). The mixed energy transfer  $\Pi_m^\ell$  is also composed of three terms:  $\Pi_{m1}^\ell$ ,  $\Pi_{m2}^\ell$  and  $\Pi_{m3}^\ell$ . The first one,  $\Pi_{m1}^\ell$ , see Eq. (2.11d), represents the energy transfer resulting from the interaction between strain at scale  $\ell$  and the strain-dilatation correlation at a scale smaller than or equal to  $\ell$ . The terms  $\Pi_{m2}^\ell$  (see Eq. (2.11e)), respectively  $\Pi_{m3}^\ell$  (see Eq. (2.11f)) describe the energy transfer resulting from the interaction between dilatation at scale  $\ell$  and strain, respectively vorticity. Finally, the dilatational energy transfer  $\Pi_d^\ell$  (see Eq. (2.11g)) arises from the interaction between dilatation at scale  $\ell$  and dilatation at a scale smaller than or equal to  $\ell$ .

We further decompose the inter-scale energy transfer terms as a sum of a scale-local ( $l$ ) and scale non-local ( $nl$ ) contributions, *i.e.*:

$$\Pi_x^\ell = \Pi_{x,l}^\ell + \Pi_{x,nl}^\ell, \quad (2.12)$$

where  $x$  denotes one of the subscripts  $s1$ ,  $s2$ ,  $s3$ ,  $m1$ ,  $m2$ ,  $m3$ , or  $d$ . The scale-local contributions involve only quantities defined at scale  $\ell$ , while the scale non-local contributions involve velocity gradients at scales finer than  $\ell$ . We find that  $\Pi_{s3,l}^\ell = 0$ , the other local contributions being expressible in terms of the five independent components of the third-order velocity gradient moment discussed in Yang *et al.* (2022):

$$\Pi_{s1,l}^\ell = \overline{\rho}^\ell \widetilde{S}_{ik}^\ell \widetilde{S}_{jk}^\ell \widetilde{S}_{ij}^\ell \ell^2, \quad (2.13a)$$

$$\Pi_{s2,l}^\ell = -\overline{\rho}^\ell \widetilde{W}_{ik}^\ell \widetilde{W}_{kj}^\ell \widetilde{S}_{ij}^\ell \ell^2, \quad (2.13b)$$

$$\Pi_{m1,l}^\ell = 2\Pi_{m2,l}^\ell = \frac{2}{3} \overline{\rho}^\ell \widetilde{S}_{ij}^\ell \widetilde{S}_{ij}^\ell \widetilde{A}_{ll}^\ell \ell^2, \quad (2.13c)$$

$$\Pi_{m3,l}^\ell = -\frac{1}{3} \overline{\rho}^\ell \widetilde{W}_{ij}^\ell \widetilde{W}_{ji}^\ell \widetilde{A}_{ll}^\ell \ell^2, \quad (2.13d)$$

$$\Pi_{d,l}^\ell = \frac{1}{9} \overline{\rho}^\ell \widetilde{A}_{ii}^\ell \widetilde{A}_{jj}^\ell \widetilde{A}_{kk}^\ell \ell^2. \quad (2.13e)$$

### 3. Numerical methods

To analyze the dilatational contribution of compressible turbulence using the approach developed above, we use DNS of freely decaying compressible homogeneous isotropic turbulence (HIT). To this end, we first solved numerically the compressible Navier-Stokes equations. In this section, we briefly introduce the governing equation, the numerical setup and the computational fluid dynamics solver. We also provide elementary information about the simulated flows.

For the non-dimensional Navier-Stokes equations, we select the reference quantities  $\rho_0$  for density,  $L_0$  for length,  $T_0$  for temperature,  $u_0$  for velocity, and  $\mu_0$  for viscosity. These five reference quantities are grouped into two dimensionless numbers: the Reynolds number  $\text{Re} = \rho_0 u_0 L_0 / \mu_0$ , which quantifies the scale separation of the flow, and the Mach number  $\text{Ma} = u_0 / \sqrt{\gamma R T_0}$  that measures the compressibility of the fluid.  $R$  is the specific gas constant and  $\gamma = 1.4$  is the ratio of specific heats. These two dimensionless numbers are set at the start of each run and remain constant throughout the simulation. The non-dimensional compressible Navier-Stokes equations are expressed as:

$$\frac{\partial \rho}{\partial t} + \frac{\partial \rho u_i}{\partial x_i} = 0, \quad (3.1a)$$

$$\frac{\partial \rho u_i}{\partial t} + \frac{\partial}{\partial x_j} (\rho u_i u_j + p \delta_{ij}) - \frac{\partial \sigma_{ij}}{\partial x_j} = 0, \quad (3.1b)$$

$$\frac{\partial \mathcal{E}}{\partial t} + \frac{\partial}{\partial x_j} [(\mathcal{E} + p) u_j] - \frac{\partial}{\partial x_j} (\sigma_{ij} u_i - Q_j) = 0, \quad (3.1c)$$

in which  $p = \rho T / (\gamma \text{Ma}^2)$  is the pressure,  $\sigma_{ij} = \mu \cdot [(\partial u_i / \partial x_j) + (\partial u_j / \partial x_i) - \frac{2}{3} (\partial u_k / \partial x_k) \delta_{ij}]$  is the non-dimensional viscous stress tensor with the effect of bulk viscosity neglected (Pan & Johnsen 2017),  $\mathcal{E} = \frac{1}{2} u_i u_i + p / (\gamma - 1)$  is the dimensionless total energy and  $Q_j = -\mu / [\text{Pr} \cdot \text{Re} (\gamma - 1) \cdot \text{Ma}^2] \cdot (\partial T / \partial x_j)$  is the dimensionless heat flux with a constant Prandtl number  $\text{Pr} = 0.72$ . The viscosity follows the Sutherland's law  $\mu = T^{3/2} \cdot (T_0 + T_{ref}) / [(T \cdot T_0 + T_{ref}) \cdot \text{Re}]$ .

Equations (3.1a)-(3.1c) are solved with a high-order finite difference method. Specifically, the convective terms are calculated by a seventh-order low-dissipative monotonicity-preserving scheme (Fang *et al.* 2013) such that shock waves in a compressible flow can be captured and the capabilities of resolving small-scale turbulent structures are preserved. The diffusion terms are discretized by a sixth-order compact central scheme (Lele 1992) with a domain decoupling scheme for parallel computation (Fang *et al.* 2019). The time integration is computed by a three-step third-order total variation diminishing Runge-Kutta method (Gottlieb & Shu 1998). For the flow simulations in this study, we utilize the open-source solver ASTR, which has been extensively validated in DNSs of various compressible turbulent flows with and without shock waves (Fang *et al.* 2013, 2014, 2015, 2016, 2020; Yang *et al.* 2022).

The computational domain for our numerical simulations is a  $(2\pi)^3$  cube with periodic conditions in all three directions, discretized with a  $512^3$  mesh. The initial velocity field is divergence-free, with an energy spectrum  $E(k) = A k^4 \exp(-2k^2/k_0^2)$ ,  $k_0 = 4$  being the wavenumber where the energy spectrum peaks and  $A$  determining the initial energy. The density,  $\rho$ , pressure,  $p$ , and temperature,  $T$ , are all initialized as constant, following the 'IC4' configuration of Samtaney *et al.* (2001). The Reynolds numbers based on the Taylor microscale is defined as  $R_\lambda = \langle \rho \rangle u' \lambda / (\sqrt{3} \langle \mu \rangle)$  and the turbulent Mach number

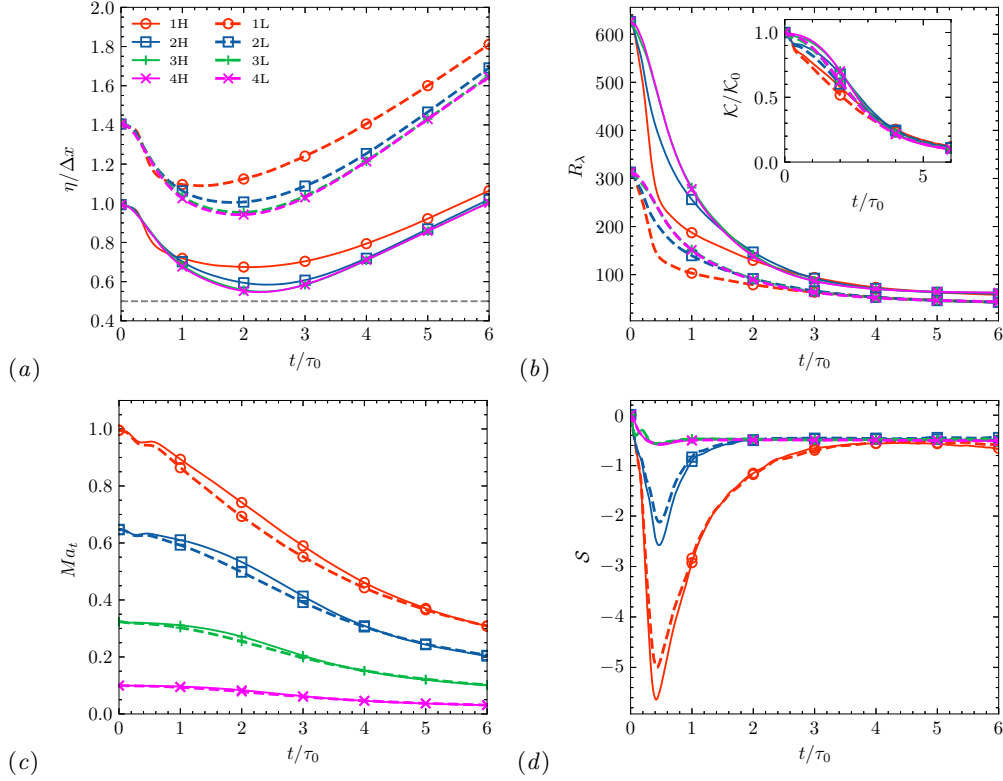


FIGURE 1. Evolution of global statistics. The solid line and dashed line refer to high and low Reynolds number runs, respectively. Red, blue, green and magenta lines refer to runs 1, 2, 3 and 4, respectively. (a) The Kolmogorov scale divided by the grid length  $\Delta x = 2\pi/512$ , the horizontal dashed line marks the threshold 0.5, (b) the Reynolds number on the Taylor microscale  $R_\lambda$  and the turbulent kinetic energy normalized by its initial value  $\mathcal{K}/\mathcal{K}_0$  (shown in the inset), (c) the turbulent Mach number  $Ma_t$ , (d) the velocity gradient skewness  $\mathcal{S}$ .

as  $Ma_t = Ma \cdot u' / \langle \sqrt{\gamma RT} \rangle$ . In the descriptions above,  $u' = \sqrt{\langle u_i u_i \rangle}$  is the root-mean-square velocity and  $\lambda = u' / \langle (\partial u_1 / \partial x_1)^2 + (\partial u_2 / \partial x_2)^2 + (\partial u_3 / \partial x_3)^2 \rangle^{1/2}$  is the Taylor microscale. We simulated in total eight flows, with four different initial turbulent Mach numbers:  $Ma_t = 1.00, 0.65, 0.32, 0.10$  (referred to as 1, 2, 3 and 4 respectively) and 2 different initial Taylor-scale Reynolds numbers  $R_\lambda = 626.21, 313.11$  (denoted in the following by H and L respectively). The main parameters characterized the simulations are summarized in Table 1. Although simulated with a compressible Navier-Stokes solver, the flows 4L and 4H can effectively be considered as incompressible, given that their Mach numbers are extremely small. In the following, we use the initial large-eddy-turnover time  $\tau_0 = (\int_0^\infty E(k)/k dk) / u'^3$  to normalize time in the simulations.

Figure 1 illustrates the evolution of global statistics. The Kolmogorov scale is defined by  $\eta = (\langle \mu / \rho \rangle^3 / \varepsilon)^{1/4}$ , with the energy dissipation rate defined as  $\varepsilon = \langle \sigma_{ij} \dot{S}_{ij} / \rho \rangle$  and  $\dot{S}_{ij} = (\partial u_i / \partial x_j + \partial u_j / \partial x_i) / 2$ . As shown in figure 1 (a), the Kolmogorov scale first decreases due to the development of strong compression. After reaching its minimum at time  $t_{\eta, \min}$ , the Kolmogorov scale  $\eta$  subsequently increases as the flow transitions into a decaying regime. After  $t_{\eta, \min}$ , figure 1 (b-c) shows that the turbulent kinetic energy  $\mathcal{K} = \langle \rho u_i u_i \rangle / 2$ , the Taylor-scale Reynolds number  $R_\lambda$  and the turbulent Mach number  $Ma_t$  all decay monotonically. Thus,  $t_{\eta, \min}$  can be regarded as the starting time of the

---

Run	Initial $R_\lambda$	Initial $Ma_t$	Initial $\eta/\Delta x$	Minimum $\eta/\Delta x$	$t_{\eta,\min}/\tau_0$
1H	626.21	1.00	0.99	0.67	2.13
2H	626.21	0.65	0.99	0.58	2.38
3H	626.21	0.32	0.99	0.55	2.30
4H	626.21	0.10	0.99	0.55	2.25
1L	313.11	1.00	1.40	1.09	1.29
2L	313.11	0.65	1.40	1.00	1.81
3L	313.11	0.32	1.40	0.95	1.94
4L	313.11	0.10	1.40	0.94	1.93

---

TABLE 1. Numerical setting and basic statistics

decay. The initial Kolmogorov scale, the minimum Kolmogorov scale, and the time of the minimal Kolmogorov scale  $t_{\eta,\min}$  are presented in Table 1,  $\Delta x$  being the grid spacing. For all runs,  $\eta/\Delta x$  remains above 0.5, ensuring adequate resolution. We also found that, during the decay, the integral scale  $L = u'^3/(\varepsilon/\langle\rho\rangle)$  remains less than one-third of the size of the computational domain (not shown), ensuring that the largest turbulent structures are adequately contained within the simulation box.

Figure 1(b) shows that the turbulent kinetic energy  $\mathcal{K}$  and the Taylor-scale Reynolds number  $R_\lambda$  all decay monotonically with time. Furthermore, while the curves of  $\mathcal{K}$  and  $R_\lambda$  deviate from each other during the initial stages, comparing flows at the same initial Reynolds number (*i.e.*, runs 1H, 2H, 3H, 4H, and runs 1L, 2L, 3L, 4L) demonstrates that the curves collapse at later time, during the decay. This observation suggests that, over the range considered here, compressibility does not significantly impact global dissipation during the decay stage. Similarly, figure 1(c) shows that the time dependence of  $Ma_t$  does not depend much on the initial Reynolds number, but rather solely on the initial Mach number. Nevertheless, in runs 1H, 2H, 3H, 1L, 2L, and 3L, despite the relatively small turbulent Mach number towards the end of the simulation, compressible effects persist in the flow field with the presence of spatially distributed shocklets in the flow. In comparison, in our simulations 4H and 4L, the flow remains incompressible throughout the calculation. The skewness of velocity gradient,  $\mathcal{S} = \langle(\partial u_1/\partial x_1)^3 + (\partial u_2/\partial x_2)^3 + (\partial u_3/\partial x_3)^3\rangle / \left( \langle(\partial u_1/\partial x_1)^2\rangle^{3/2} + \langle(\partial u_2/\partial x_2)^2\rangle^{3/2} + \langle(\partial u_3/\partial x_3)^2\rangle^{3/2} \right)$ , shown in Fig. 1(d), exhibits a sharp negative peak for runs 1L, 2L, 1H, and 2H at approximately  $t/\tau_0 \approx 0.35$ , reflecting the transient from the initial divergence-free velocity field to a compressible flow field. In contrast, for runs 3H, 3L, 4H, and 4L, the skewness decreases during the initial stage. Once the turbulent regime is well established, the skewness remains nearly constant at approximately  $-\mathcal{S} \approx 0.5$ , which aligns with the theoretical estimates for incompressible turbulence as described in Qian (1994). Overall, our results are consistent with the scaling proposed by Donzis & John (2020).

#### 4. Numerical study of the energy flux

In this section, we begin by validating the SGS stress integral expression Eq. (2.9), and we study the total inter-scale energy transfers, see §4.1. Furthermore, in §4.2, we present a systematic analysis for the solenoidal and dilatational contributions. We also investigate the scaling of the dilatational contribution as a function of the turbulent Mach number in §4.3. Finally, we apply our results to the LES and discuss the limitations of the current SGS viscosity model in §4.4.



---

Run	$R_\lambda$	$Ma_t$	$\eta/\Delta x$	$\lambda/\eta$	$L/\eta$	$\mathcal{S}$
1H	59.68	0.33	1.00	14.74	181.92	-0.62
2H	61.56	0.22	0.96	15.12	187.21	-0.50
3H	62.87	0.11	0.95	15.56	186.35	-0.49
4H	63.06	0.03	0.94	15.62	185.98	-0.51
1L	43.95	0.33	1.72	12.67	114.31	-0.56
2L	44.24	0.22	1.60	12.89	112.79	-0.46
3L	43.90	0.11	1.56	13.00	108.68	-0.48
4L	44.13	0.03	1.56	13.05	109.44	-0.51

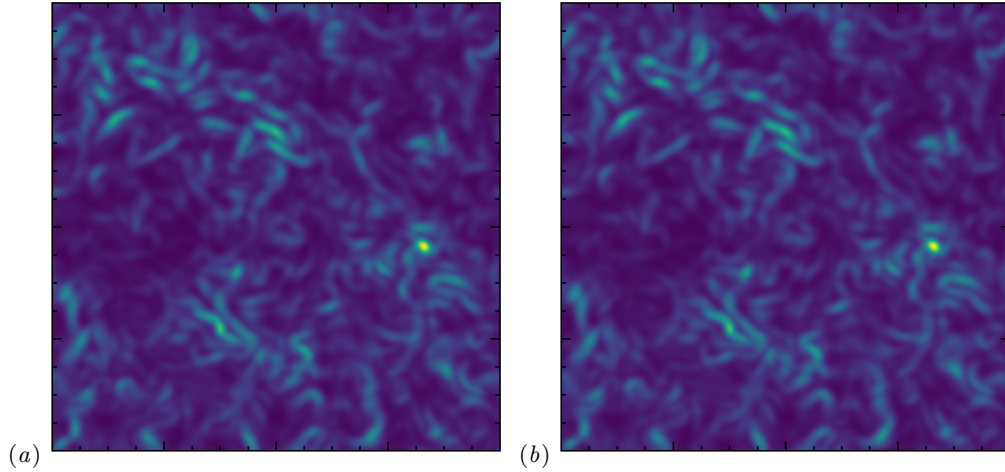
---

TABLE 2. Global statistics at the moment  $t/\tau_0 = 5.59$ .

---

$\ell$	Average relative errors(%)						$\ \tau^\ell\ _F^2 = \tau_{ij}^\ell \tau_{ij}^\ell$
	$\tau_{11}^\ell$	$\tau_{22}^\ell$	$\tau_{33}^\ell$	$\tau_{12}^\ell$	$\tau_{13}^\ell$	$\tau_{23}^\ell$	
$4.90\eta$	0.43	0.43	0.43	0.34	0.34	0.34	0.71
$15.58\eta$	0.86	0.87	0.88	0.78	0.78	0.76	1.66

---

TABLE 3. Average relative errors (%) of the SGS stress calculated with the integral expression  $\tau_{ij,\text{int}}^\ell$  with respect to the SGS stress calculated with the definition  $\tau_{ij,\text{def}}^\ell$ , for the run 1H at  $t/\tau_0 = 5.59$ .FIGURE 2. A SGS stress  $\tau_{11}^\ell$  of the section  $x = \pi$  for the run 1H filtered at the scale  $\ell = 4.90\eta$ . Both figures use the same color map. (a) With the definition  $\tau_{11,\text{def}}^\ell$ . (b) With the integral expression  $\tau_{11,\text{int}}^\ell$ .

#### 4.1. Validation of Eq. (2.9) and study of total inter-scale energy transfer

In this subsection and in the next one, we focus mostly on the flow field at a single moment in the stable decaying regime, namely  $t/\tau_0 = 5.59$ , to study the SGS stress and inter-scale energy transfer. Table 2 lists some of the essential global statistical quantities at the selected time. Note that at this moment, the turbulent Mach numbers  $Ma_t$  in all runs satisfy  $Ma_t \lesssim 0.3$  and correspond to the low- $Ma_t$  regime (Jagannathan & Donzis 2016).

First, we validate the integral expression of SGS stress by calculating it using Eqs. (2.1)

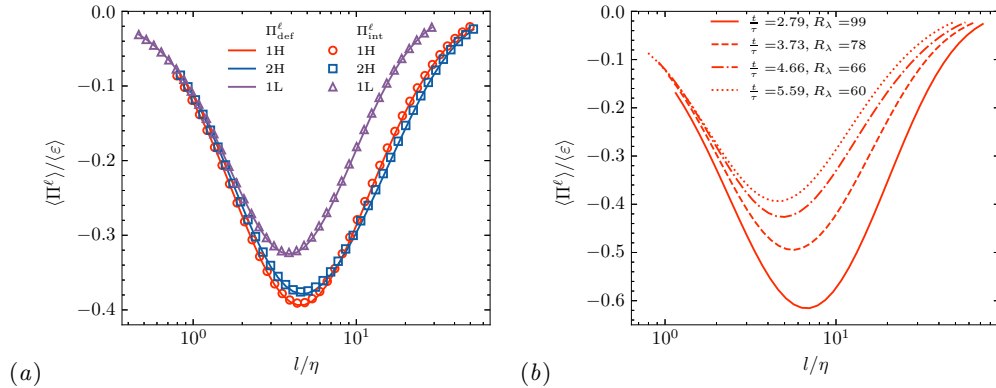


FIGURE 3. Total inter-scale energy transfer  $\langle \Pi^\ell \rangle$  as a function of filtering scale  $\ell$ . All quantities are normalized by the average energy dissipation rate  $\langle \epsilon \rangle$ . (a) At  $t/\tau_0 = 5.59$  for runs 1H, 2H and 1L. Solid lines represent the energy transfer calculated from the definition  $\Pi_{\text{def}}^\ell$ , and symbols represent the energy transfer calculated from the integral expression  $\Pi_{\text{int}}^\ell$ . (b) At different moments for run 1H.

and (2.9). The standard rectangle method is employed for the numerical integration in Eq. (2.9), with sufficiently small steps to ensure convergence. The quantities obtained from the integral expressions differ from the definition, Eq. (2.1) by of the order of 1%. Typical values of the norm of the differences are shown in Table 3, at two values of  $\ell$ . In addition, figure 2 shows the SGS stress  $\tau_{11}^\ell$  in the plane  $x = \pi$  for run 1H at  $t/\tau_0 = 5.59$ , filtered at the scale  $\ell = 4.90\eta$ . In Figure 2(a), we represent the value of  $\tau_{11}^\ell$  determined using the definition, Eq. (2.1), and in Figure 2(b), the result of the integral expression, Eq. (2.9). The comparison between the two panels demonstrates that the integral expression Eq. (2.9) accurately represents the SGS stress, as defined by Eq. (2.1). This demonstrates the quality of our numerical results.

Figure 3 shows the dependence of the total inter-scale energy transfer  $\langle \Pi^\ell \rangle$  on the filtering scale  $\ell$  for runs 1H, 2H and 1L, at  $Ma_t$  respectively 0.33, 0.22 and 0.33. The solid lines represent the calculations from the definition  $\Pi_{\text{def}}^\ell \equiv \tau_{ij}^\ell \frac{\partial \tilde{u}_i^\ell}{\partial x_j}$  and the symbols correspond to the integral expression of Eq. (2.10). For all runs and all filtering scales, the solid line and symbols agree with each other to within 2%, further validating the numerical integration of the SGS stress. We found a similar agreement for all the other runs (not shown).

Additionally, we observe that the maximum of  $|\langle \Pi^\ell \rangle / \langle \epsilon \rangle|$  is significantly smaller than 1, whereas in the forced steady-state turbulence simulations of Johnson (2020) (see Fig. 2 of this article), this ratio is found to be very close to 1. This can be attributed to the different numerical setups. In Johnson (2020), energy is continuously injected at large scales, resulting in a forced steady case, with a balance between energy transfer  $\langle \Pi^\ell \rangle$  and dissipation  $\langle \epsilon \rangle$ . In contrast, we simulate freely decaying turbulence, where the energy transferred through a certain scale in the inertial range is dissipated later at smaller scales. Consequently, the energy transfer rate at any scale is always lower than the dissipation rate at any given time due to the overall decrease in total energy. Furthermore, viscosity plays a more important role at the low values of  $R_\lambda$  considered here, leading to smaller maximum values of  $|\langle \Pi^\ell \rangle / \langle \epsilon \rangle|$  at lower Reynolds number runs. This is evident when comparing the curves of runs 1H and 1L in 3(a). A similar trend is observed in figure 3(b), which shows the energy transfer at four different time instances for run 1H. As time progresses and the Taylor microscale Reynolds number decreases,

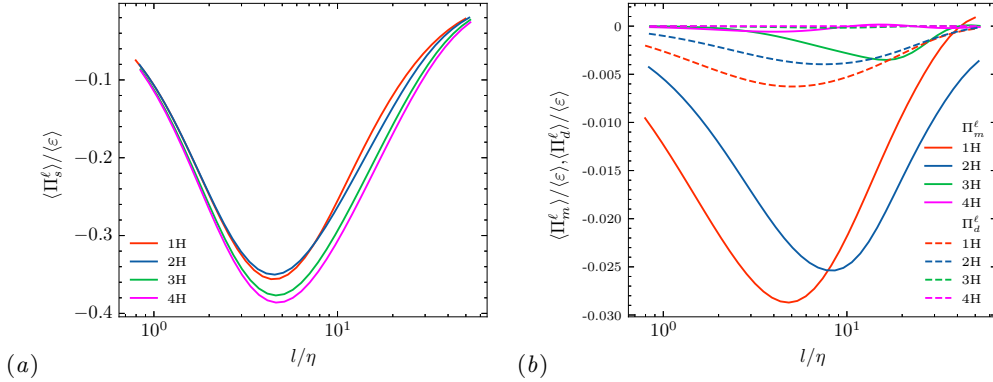


FIGURE 4. Average inter-scale energy transfer as a function of filtering scale  $\ell$ . Red, blue, green and magenta lines refer to runs 1H, 2H, 3H, and 4H, respectively. All curves are normalized by the average energy dissipation rate  $\langle \epsilon \rangle$ . (a) Energy transfer within the solenoidal part  $\langle \Pi_s^\ell \rangle$  at  $t/\tau_0 = 5.59$  for the different runs. (b) Energy transfer between the solenoidal part and the dilatational part  $\langle \Pi_m^\ell \rangle$  (solid line) and within the dilatational part  $\langle \Pi_d^\ell \rangle$  (dashed line) at  $t/\tau_0 = 5.59$  for the different runs.

the peak value of  $\langle \Pi^\ell \rangle / \langle \epsilon \rangle$  as a function of  $\ell$  also diminishes. We notice in this respect that the values of  $R_\lambda \approx 400$  in the work of Johnson (2020) is significantly higher than ours.

#### 4.2. Solenoidal and dilatational contribution to inter-scale energy flux

In this subsection, we analyze the solenoidal and dilatational contributions to the energy flux by examining the different terms of the inter-scale energy transfer for high Reynolds number runs over the range of Mach numbers covered by our study: runs 1H ( $Ma_t = 0.33$ ), 2H ( $Ma_t = 0.22$ ), 3H ( $Ma_t = 0.11$ ), and 4H ( $Ma_t = 0.03$ ). Similar trends are observed at lower Reynolds numbers (runs 1L-4L).

Figure 4 shows the dependence on scale,  $\ell$ , of the various contributions to the inter-scale energy transfer. Specifically, panel (a) shows the contribution due to the solenoidal component,  $\Pi_s^\ell$ , and panel (b) the result of the interaction between the solenoidal and the dilatational components,  $\Pi_m^\ell$ , as well as the contribution induced by the purely dilatational part,  $\Pi_d^\ell$ . As expected,  $\langle \Pi_m^\ell \rangle$  and  $\langle \Pi_d^\ell \rangle$  are very close to zero for run 4H ( $Ma_t = 0.03$ ), and increase with the turbulent Mach number. For runs 1H, 2H, and 3H,  $\langle \Pi_s^\ell \rangle$  is significantly larger than  $\langle \Pi_m^\ell \rangle$  and  $\langle \Pi_d^\ell \rangle$ , indicating that the energy transfer is mostly due to the solenoidal motion. This is a consequence of the relatively small values of the corresponding turbulent Mach number ( $Ma_t \lesssim 0.3$ ), which is not expected to be valid beyond the low  $Ma_t$  regime. Furthermore, all terms are negative at small scales ( $\ell \ll L$ ), demonstrating that in 3D freely decaying compressible turbulence, all terms contribute to an energy cascade from large to small scales.

Next, we consider separately all terms contributing to the inter-scale energy transfer, see Section 2. Figure 5 shows the contribution of each term to the inter-scale energy transfer within the solenoidal part, as studied in the incompressible case (Johnson 2020; Yang *et al.* 2023). Figure 5 exhibits trends similar to those observed in figure 3 of Johnson (2020). This suggests that in the regime of  $Ma_t$  considered here, compressibility has a small influence on the energy transfer associated with the solenoidal component of the velocity. The Betchov identities (Betchov 1956) imply that  $\langle \Pi_{s1,l}^\ell \rangle = 3 \langle \Pi_{s2,l}^\ell \rangle$ , for the scale-local terms in homogeneous flows. For scale non-local interactions, the approxima-

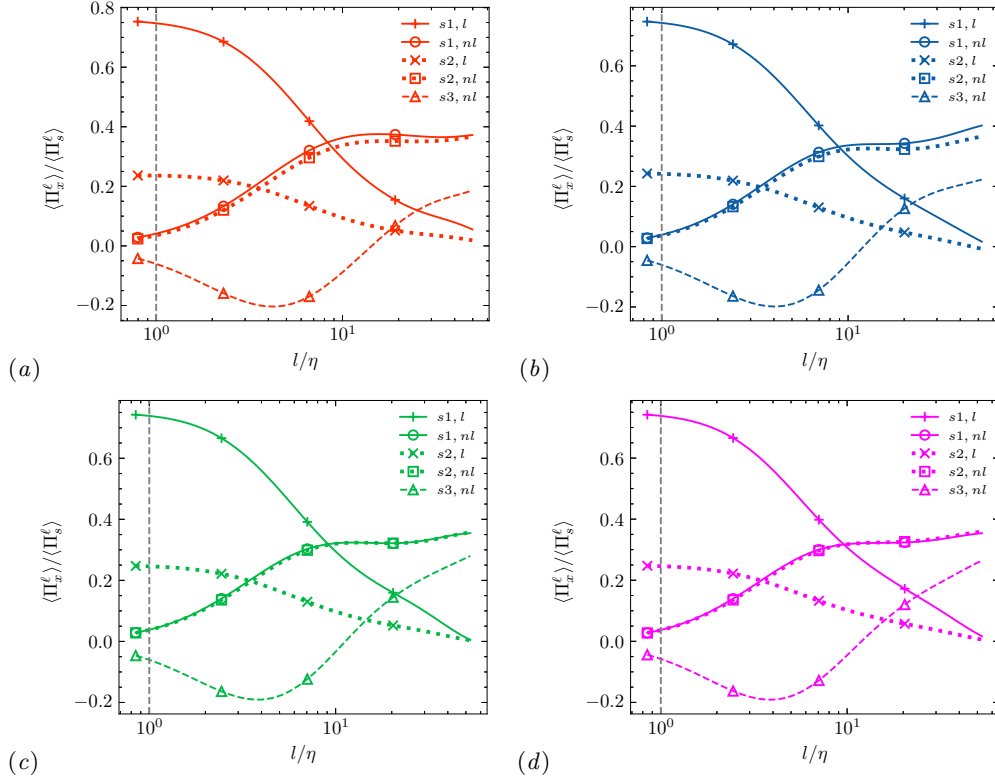


FIGURE 5. Various terms of the inter-scale energy transfer within the solenoidal mode as a function of filtering scale  $\ell$  for the runs at  $t/\tau_0 = 5.59$ , normalized by the sum of these terms  $\langle \Pi_s^\ell \rangle$ . The gray dashed line indicates the scale  $\ell = \eta$ . (a) Run 1H ( $Ma_t = 0.33$ ), (b) Run 2H ( $Ma_t = 0.22$ ), (c) Run 3H ( $Ma_t = 0.11$ ), (d) Run 4H ( $Ma_t = 0.03$ ). The structure of the energy transfer due to the solenoidal component of the flow is relatively insensitive to the turbulent Mach number over the range covered by our study.

tion of  $\langle \Pi_{s1,nl}^\ell \rangle \approx \langle \Pi_{s2,nl}^\ell \rangle$  holds for all  $\ell$ , consistent with the numerical observations of Johnson (2020), see also the theoretical discussion of Yang *et al.* (2023). Furthermore, when  $\ell \lesssim \eta$ , the energy transfer is dominated by local terms, the non-local terms being comparatively small. Specifically, at  $\ell = \eta$ , the three non-local terms  $\Pi_{s1,nl}^\ell$ ,  $\Pi_{s2,nl}^\ell$ , and  $\Pi_{s3,nl}^\ell$  account for approximately 4%, 4%, and  $-6\%$  of the total solenoidal energy transfer, respectively. This indicates that non-local energy transfer at scales below  $\eta$  is very weak. Consequently, numerical simulations with a grid size of the order of  $\eta$  correctly represent the energy transfer due to the solenoidal energy. This is consistent with the classical spatial resolution criterion for DNS, *i.e.*,  $\Delta x \lesssim 2\eta$ .

However, at larger scales ( $\ell \gg \eta$ ), non-local contributions dominate the local ones, accounting for almost the total solenoidal inter-scale energy transfer. This result differs from Johnson (2020), which found that  $\langle \Pi_{s,l}^\ell \rangle \approx \langle \Pi_{s,nl}^\ell \rangle$ . This discrepancy may be attributed to the different Reynolds numbers (with  $R_\lambda < 100$  in our work and  $R_\lambda = 400$  in Johnson (2020)) and the different flow types (freely decaying turbulence here versus forced steady flow in Johnson (2020)), which may influence the structure of the large-scale flow (Yang *et al.* 2018).

Figure 6 shows the relative contributions of each term to the inter-scale energy transfer due to the interaction between the solenoidal and dilatational components. The structure

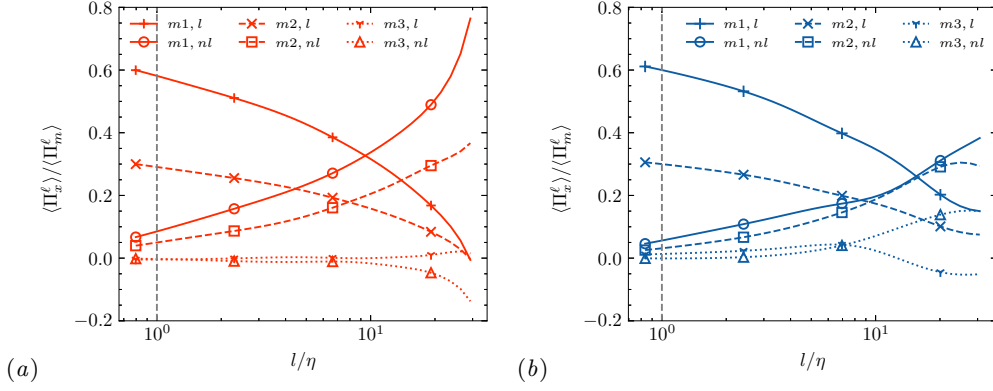


FIGURE 6. Terms of the inter-scale energy transfer between the solenoidal part and the dilatational part as a function of filtering scale  $\ell$  at  $t/\tau_0 = 5.59$ , normalized by the sum of these terms  $\langle \Pi_m^\ell \rangle$ . The gray dashed line shows the scale  $\ell = \eta$ . (a) Run 1H ( $Ma_t = 0.33$ ), (b) run 2H ( $Ma_t = 0.22$ ).

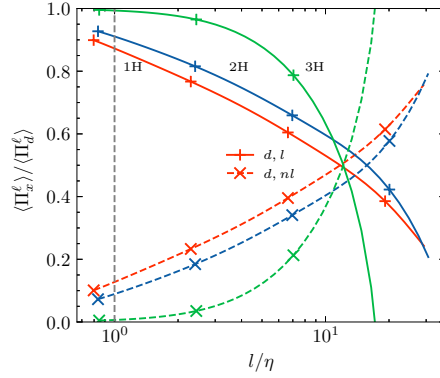


FIGURE 7. Terms of the inter-scale energy transfer within the dilatational part as a function of filtering scale  $\ell$  at  $t/\tau_0 = 5.59$ , normalized by the sum of these terms  $\langle \Pi_d^\ell \rangle$ . Red, blue and green lines refer to runs 1H, 2H, and 3H, respectively. The gray dashed line shows the scale  $\ell = \eta$ .

of the solution is shown for run 1H, panel (a) and for run 2H, panel (b). For  $\ell \lesssim \eta$ , the local terms  $\langle \Pi_{m1,l}^\ell \rangle$  and  $\langle \Pi_{m2,l}^\ell \rangle$  dominate the energy transfer, with a ratio between the local contributions, defined by Eq. (2.13c),  $\langle \Pi_{m1,l}^\ell \rangle : \langle \Pi_{m2,l}^\ell \rangle = 2 : 1$ . Notably, at  $\ell = \eta$ , the contributions of the non-local terms,  $\Pi_{m1,nl}^\ell$  and  $\Pi_{m2,nl}^\ell$ , are approximately 8% and 5% of the total solenoidal-dilatational energy transfer, respectively. This is larger than the non-local contributions induced by the solenoidal component. At large scales ( $\ell \gg \eta$ ), the inter-scale energy transfer is dominated by the non-local term  $\langle \Pi_{m1,nl}^\ell \rangle$  involving strain and dilatation. The interaction between dilatation and vorticity, described by the term  $\langle \Pi_{m3}^\ell \rangle$ , contributes very little to the energy transfer. This is consistent with previous observations that vorticity and dilatation are nearly uncorrelated in compressible homogeneous turbulence and have a small contribution to energy transfer (Erlebacher & Sarkar 1993; Wang *et al.* 2012a; Yang *et al.* 2022). The relatively large values of  $\langle \Pi_{m3,l}^\ell \rangle$  and  $\langle \Pi_{m3,nl}^\ell \rangle$  in figure 6(b) at large scales may be a special property of the individual configuration considered here.

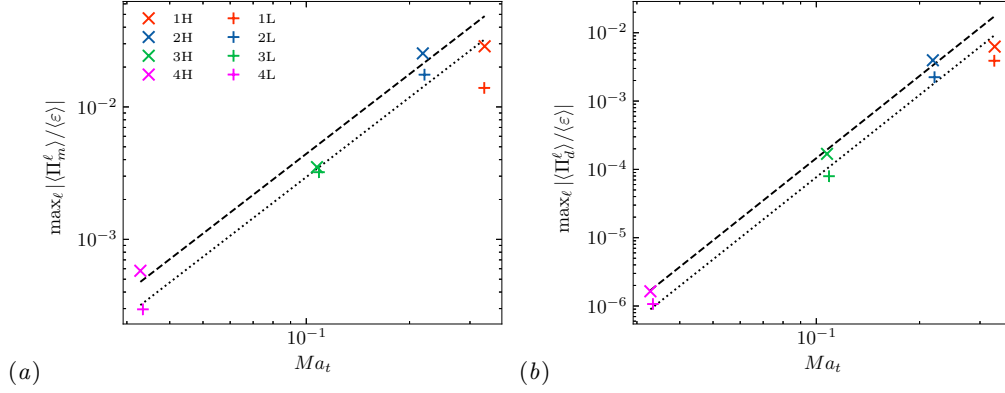


FIGURE 8. The maximum inter-scale energy transfer  $\max_\ell |\langle \Pi_x^\ell \rangle / \langle \varepsilon \rangle|$  as a function of turbulent Mach number  $Ma_t$  at  $t/\tau = 5.59$ . Both axis are in logarithmic scale. ‘x’ symbol and ‘+’ symbol refer to high and low Reynolds number runs, respectively. Red, blue, green and magenta symbols refer to runs 1, 2, 3, and 4, respectively. The black dashed line and the black dotted line are the linear regression of data of runs 2H, 3H, 4H and 2L, 3L, 4L, respectively. (a) Inter-scale energy transfer caused by the solenoidal-dilatational interaction  $\max_\ell |\langle \Pi_m^\ell \rangle / \langle \varepsilon \rangle|$ . (b) Inter-scale energy transfer caused by the dilatational motion  $\max_\ell |\langle \Pi_d^\ell \rangle / \langle \varepsilon \rangle|$ .

Figure 7 shows the relative contributions of the local and non-local terms to the inter-scale energy transfer,  $\langle \Pi_{d,l}^\ell \rangle$  and  $\langle \Pi_{d,nl}^\ell \rangle$ , due to the dilatational component. As it was the case for  $\langle \Pi_s^\ell \rangle$  and  $\langle \Pi_m^\ell \rangle$ , the local contribution dominates at small scales, for ( $\ell \lesssim \eta$ ), and decreases when  $\ell$  increases, while the non-local contribution is close to 0 at small scales and increases with  $\ell$ . Notably, at  $\ell = \eta$ ,  $\langle \Pi_{d,nl}^\ell \rangle / \langle \Pi_d^\ell \rangle$  is 13% for run 1H, 9% for run 2H and less than 1% for the run 3H. This ratio manifestly increases with the Mach number,  $Ma_t$ , and is greater than  $(\langle \Pi_{s1,nl}^\ell \rangle + \langle \Pi_{s2,nl}^\ell \rangle + \langle \Pi_{s3,nl}^\ell \rangle) / \langle \Pi_s^\ell \rangle$ , which is the non-local contribution observed in the solenoidal energy transfer. This signifies that the non-local motions at scales smaller than  $\eta$  play a more significant role in the dilatational energy transfer at  $\eta$ . The implication for numerical simulations is that even with a grid size of the order of  $\eta$ , uncertainties in  $\langle \Pi_{d,nl}^\eta \rangle$  may significantly affect the energy transfer due to the dilatational component of the velocity. This implies, in turn, that the classical spatial resolution criteria based on the Kolmogorov scale may not be sufficient to accurately capture the effect of the dilatational terms.

### 4.3. Scaling of dilatational contribution with Mach number

In this subsection, we study the relationship between the dilatational component of the inter-scale energy transfer and the turbulent Mach number.

For each run, we compute the maximum inter-scale energy transfer  $|\langle \Pi_x^\ell \rangle / \langle \varepsilon \rangle|$  with  $x = m$  and  $d$  as a function of  $\ell$ . Figures 8(a) and 8(b) show this maximum value at  $t/\tau = 5.59$  as a function of the turbulent Mach number. The data in figure 8(a) can be fitted as  $\max_\ell |\langle \Pi_m^\ell \rangle / \langle \varepsilon \rangle| \approx 0.44 Ma_t^2$  for runs 2H, 3H and 4H, and  $\max_\ell |\langle \Pi_m^\ell \rangle / \langle \varepsilon \rangle| \approx 0.30 Ma_t^2$  for runs 2L, 3L and 4L. Similarly, the data in figure 8(b) can be fitted as  $\max_\ell |\langle \Pi_d^\ell \rangle / \langle \varepsilon \rangle| \approx 1.46 Ma_t^4$  for runs 2H, 3H and 4H, and as  $\max_\ell |\langle \Pi_d^\ell \rangle / \langle \varepsilon \rangle| \approx 0.77 Ma_t^4$  for runs 2L, 3L and 4L. Both  $\max_\ell |\langle \Pi_m^\ell \rangle / \langle \varepsilon \rangle|$  and  $\max_\ell |\langle \Pi_d^\ell \rangle / \langle \varepsilon \rangle|$  are increasing functions of the turbulent Mach number and vary respectively as  $\sim Ma_t^2$  and  $\sim Ma_t^4$ . The prefactors of the scaling laws appear to be increasing with the Reynolds numbers. Notably, runs 1H and 1L deviate from the regression lines, suggesting that

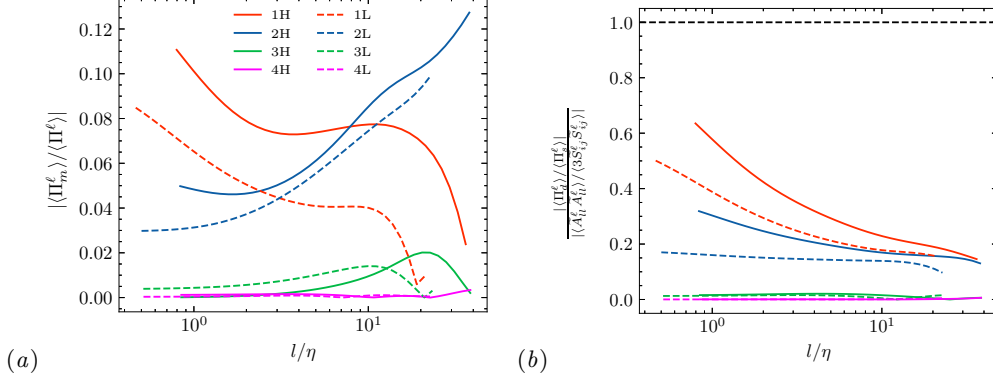


FIGURE 9. Critical ratios as a function of the filtering scale  $\ell$  at  $t/\tau_0 = 5.59$ . The solid line and dashed line refer to high and low Reynolds number runs, respectively. Red, blue, green and magenta lines refer to runs 1, 2, 3, and 4, respectively. (a) The ratio of  $\langle \Pi_m^\ell \rangle / \langle \Pi^\ell \rangle$ . (b) The ratio of  $|\langle \Pi_d^\ell \rangle / \langle \Pi_s^\ell \rangle| / \left| \langle \tilde{A}_{ll}^\ell \tilde{A}_{ll}^\ell \rangle / \langle 3\tilde{S}_{ij}^\ell \tilde{S}_{ij}^\ell \rangle \right|$ . The black dashed line shows the reference value 1.

the scaling laws apply only in the low- $Ma_t$  regime of compressible turbulence, with a turbulent Mach number  $Ma_t \lesssim 0.3$ .

#### 4.4. Examination on the eddy-viscosity assumption in LES modeling

When the turbulent Mach number is relatively low ( $Ma_t \lesssim 0.3$ ), the solenoidal modes are expected to contain most of the turbulent kinetic energy (Garnier *et al.* 2013). In this low- $Ma_t$  regime, the Boussinesq eddy-viscosity assumption (Boussinesq 1877) could be extended to the compressible LES, suggesting the following expression for the SGS stress (Garnier *et al.* 2013):

$$\tau_{ij}^\ell = -\bar{\rho}^\ell \nu_{sgs} \left( \frac{\partial \tilde{u}_i^\ell}{\partial x_j} + \frac{\partial \tilde{u}_j^\ell}{\partial x_i} \right) = -2\bar{\rho}^\ell \nu_{sgs} \left( \tilde{S}_{ij}^\ell + \frac{\tilde{A}_{ll}^\ell \delta_{ij}}{3} \right), \quad (4.1)$$

used in many classical LES models, such as the Smagorinsky model (Smagorinsky 1963), the mixed scales model (Yoshizawa 1986), and the structure function model (Sagaut 1995).

Here, we discuss a limitation of this assumption in LES of compressible flows. By substituting the eddy-viscosity assumption into the definition of inter-scale energy transfer, we could get the modeled inter-scale energy transfer as:

$$\Pi_{ev}^\ell = \underbrace{-2\bar{\rho}^\ell \nu_{sgs} \tilde{S}_{ij}^\ell \tilde{S}_{ij}^\ell}_{\Pi_{s,ev}^\ell} - \underbrace{\frac{2}{3}\bar{\rho}^\ell \nu_{sgs} \tilde{A}_{ll}^\ell \tilde{A}_{ll}^\ell}_{\Pi_{d,ev}^\ell}, \quad (4.2)$$

where the “ev” in the subscript signifies eddy-viscosity. The eddy-viscosity assumption is theoretically valid only if the real inter-scale energy transfer and the modeled one are equal. By comparing Eq. (2.10) and Eq. (4.2), it can be concluded that there are two requirements for the eddy-viscosity assumption:

- For the chosen filtering scale  $\ell$ ,  $\langle \Pi_m^\ell \rangle$  should be negligible comparing with  $\langle \Pi^\ell \rangle$ .
- For the chosen filtering scale  $\ell$ , the ratio of energy transfer  $\langle \Pi_d^\ell \rangle / \langle \Pi_s^\ell \rangle$  and of filtered velocity gradient moment  $\langle \tilde{A}_{ll}^\ell \tilde{A}_{ll}^\ell \rangle / \langle 3\tilde{S}_{ij}^\ell \tilde{S}_{ij}^\ell \rangle$  should be the same.

For our numerical cases, Figure 9(a) shows the dependence on the filtering scale,  $\ell$ , of

the ratio  $\langle \Pi_m^\ell \rangle / \langle \Pi^\ell \rangle$  obtained from our simulations. For runs 1H, 1L, 2H, and 2L, corresponding to  $Ma_t \gtrsim 0.2$ ,  $\langle \Pi_m^\ell \rangle$  accounts for more than 4% for the total inter-scale energy transfer, which is not captured by the SGS viscosity model. Besides, figure 9(b) shows a discrepancy between the fraction of the modeled energy transfer ( $\langle \Pi_{d,ev}^\ell \rangle / \langle \Pi_{s,ev}^\ell \rangle$ ) and the actual energy transfer ( $\langle \Pi_d^\ell \rangle / \langle \Pi_s^\ell \rangle$ ). As a result, the eddy-viscosity assumption leads to an overestimation on the dilatational effects. These observations highlight the limitations of the direct application of the eddy-viscosity assumption to compressible flows, and suggest potential directions for improving future SGS modeling techniques.

## 5. Concluding Remarks

In summary, we derived an integral expression for subgrid-scale (SGS) stress of compressible turbulence and introduced a methodology to analyze inter-scale energy transfer. This allows us to formally decompose the kinetic energy transfer into components associated with solenoidal motion, solenoidal-dilatational interaction, and dilatational motion, which are further categorized into scale-local and non-local contributions.

Our theoretical decomposition is validated through DNS of freely decaying compressible turbulence. The results reveal that at moderate turbulent Mach number,  $Ma_t \lesssim 0.3$ , the energy transfer due to the solenoidal component of the flow follows a pattern similar to that observed in incompressible turbulence, and is not particularly sensitive to the turbulent Mach number,  $Ma_t$ . Our analysis of the contributions of the different terms for the energy transfer due to the interaction between solenoidal and dilatational, and to the dilatational components shows that non-local dilatational motions smaller than the Kolmogorov scale contribute substantially to the energy transfer. This suggests that traditional spatial resolution criteria of DNS for incompressible turbulence may be insufficient for compressible turbulence, even at moderate turbulent Mach number. Additionally, for weakly compressible turbulence, we observed that  $\max_\ell |\langle \Pi_m^\ell \rangle / \langle \varepsilon \rangle|$  and  $\max_\ell |\langle \Pi_d^\ell \rangle / \langle \varepsilon \rangle|$  scale with the turbulent Mach number as  $Ma_t^2$  and  $Ma_t^4$ , highlighting the impact of compressibility on energy transfer dynamics. Our study also identifies limitations of the eddy-viscosity assumption when applied to large-eddy simulations (LES) of compressible turbulence. Specifically, this assumption tends to ignore energy transfer associated with solenoidal-dilatational interactions while overestimating dilatational effects. This discrepancy suggests the potential directions for improving future SGS modeling techniques to more accurately capture the complex interactions in compressible turbulence.

## Acknowledgements

PFY, HX and LF acknowledge support from the National Natural Science Foundation of China (NSFC) under grants 12202452, 11672157, 91852104 and 12372214. JF acknowledges the UK Engineering and Physical Sciences Research Council (EPSRC) through the Computational Science Centre for Research Communities (CoSeC), and the UK Turbulence Consortium (No. EP/R029326/1). AP was supported by the French Agence Nationale de la Recherche under Contract No. ANR-20-CE30-0035 (project TILT), and is thankful to the Max Planck Institute for Dynamics and Self-organisation (Göttingen, Germany) for its continuous support.

**Declaration of Interest:** The authors report no conflict of interest.



## REFERENCES

- ALUIE, H. 2011 Compressible turbulence : The cascade and its locality. *Phys. Rev. Lett.* **106**, 174502.
- ALUIE, H. 2013 Scale decomposition in compressible turbulence. *Physica D* **247**, 54–65.
- ALUIE, H., LI, S. & LI, H. 2012 Conservative cascade of kinetic energy in compressible turbulence. *Astrophys. J. Lett.* **751**, L29.
- BALLOUZ, J. G. & OUELLETTE, N. T. 2018 Tensor geometry in the turbulent cascade. *J. Fluid Mech.* **835**, 1048–1064.
- BALLOUZ, J. G. & OUELLETTE, N. T. 2020 Geometric constraints on energy transfer in the turbulent cascade. *Phys. Rev. Fluids* **5**, 034603.
- BANERJEE, S. & GALTIER, S. 2014 A Kolmogorov-like exact relation for compressible polytropic turbulence. *J. Fluid Mech.* **742**, 230–242.
- BATAILLE, F. & ZHOU, Y. 1999 Nature of the energy transfer process in compressible turbulence. *Phys. Rev. E* **59**, 5417–5426.
- BETCHOV, R. 1956 An inequality concerning the production of vorticity in isotropic turbulence. *J. Fluid Mech.* **1**, 497–504.
- BILLIG, F. S. 1988 Combustion processes in supersonic flow. *J. Propuls. Power* **4**, 209–216.
- BOUSSINESQ, J. 1877 *Essai sur la théorie des eaux courantes*. Imprimerie nationale.
- CAPOCCI, D., JOHNSON, P. L., OUGHTON, S., BIFERALE, L. & LINKMANN, M. 2023 New exact Betchov-like relation for the helicity flux in homogeneous turbulence. *J. Fluid Mech.* **963**, R1.
- CHAI, X. & MAHESH, K. 2012 Dynamic-equation model for large-eddy simulation of compressible flows. *J. Fluid Mech.* **699**, 385–413.
- CHERNYSHOV, A. A., KARELSKY, K. V. & PETROSYAN, A. S. 2010 Weakly compressible turbulence in local interstellar medium. three-dimensional modeling using large eddy simulation method. In *AIP Conf.*, , vol. 1242, pp. 197–204. American Institute of Physics.
- CURRAN, E., HEISER, W. & PRATT, D. 1996 Fluid phenomena in scramjet combustion systems. *Annu. Rev. Fluid Mech.* **28**, 323–360.
- DAVIDSON, P. A. 2015 *Turbulence: An Introduction for Scientists and Engineers (2nd edition)*. Oxford University Press.
- DONG, S., HUANG, Y., YUAN, X. & LOZANO-DURÁN, A. 2020 The coherent structure of the kinetic energy transfer in shear turbulence. *J. Fluid Mech.* **892**, A22.
- DONZIS, D. A. & JOHN, J. P. 2020 Universality and scaling in homogeneous compressible turbulence. *Phys. Rev. Fluids* **5**, 084609.
- ELMEGREEN, B. G. & SCALO, J. 2004 Interstellar turbulence I: observations and processes. *Annu. Rev. Astron. Astrophys.* **42**, 211–273.
- ERLEBACHER, G. & SARKAR, S. 1993 Statistical analysis of the rate of strain tensor in compressible homogeneous turbulence. *Phys. Fluids* **5**, 3240–3254.
- EYINK, G. 2006 Multi-scale gradient expansion of the turbulent stress tensor. *J. Fluid Mech.* **549**, 159–190.
- EYINK, G. L. & DRIVAS, T. D. 2018 Cascades and dissipative anomalies in compressible fluid turbulence. *Phys. Rev. X* **8**, 011022.
- FALKOVICH, G., FOUXON, I. & OZ, Y. 2010 New relations for correlation functions in Navier-Stokes turbulence. *J. Fluid Mech.* **644**, 465–472.
- FALKOVICH, G. & KRITSUK, A. G. 2017 How vortices and shocks provide for a flux loop in two-dimensional compressible turbulence. *Phys. Rev. Fluids* **2**, 092603.
- FANG, J., GAO, F., MOULINEC, C. & EMERSON, D. 2019 An improved parallel compact scheme for domain-decoupled simulation of turbulence. *Int. J. Numer. Methods Fluids* **90**, 479–500.
- FANG, J., LI, Z. & LU, L. 2013 An optimized low-dissipation monotonicity-preserving scheme for numerical simulations of high-speed turbulent flows. *J. Sci. Comput.* **56**, 67–95.
- FANG, J., YAO, Y., LI, Z. & LU, L. 2014 Investigation of low-dissipation monotonicity-preserving scheme for direct numerical simulation of compressible turbulent flows. *Comput. Fluids* **104**, 55–72.
- FANG, J., YAO, Y., ZHELTOVODOV, A. A., LI, Z. & LU, L. 2015 Direct numerical simulation of supersonic turbulent flows around a tandem expansion-compression corner. *Phys. Fluids* **27**, 125104.

- FANG, J., ZHELTOVODOV, A. A., YAO, Y., MOULINEC, C. & EMERSON, D. R. 2020 On the turbulence amplification in shock-wave/turbulent boundary layer interaction. *J. Fluid Mech.* **897**, A32.
- FANG, L., ZHANG, Y., FANG, J. & ZHU, Y. 2016 Relation of the fourth-order statistical invariants of velocity gradient tensor in isotropic turbulence. *Phys. Rev. E* **94**, 023114.
- FAUCHET, G. 1998 Modélisation en deux points de la turbulence isotrope compressible et validation à l'aide de simulations numériques. PhD thesis, L'Université Claude Bernard-Lyon 1.
- FERRAND, R., GALTIER, S., SAHRAOUI, F. & FEDERRATH, C. 2020 Compressible turbulence in the interstellar medium: New insights from a high-resolution supersonic turbulence simulation. *Astrophys. J.* **904**, 160.
- FRISCH, U. 1995 *Turbulence: The Legacy of A. N. Kolmogorov*. Cambridge, England: Cambridge University Press.
- GALTIER, S. & BANERJEE, S. 2011 Exact relation for correlation functions in compressible isothermal turbulence. *Phys. Rev. Lett.* **107**, 134501.
- GARNIER, E., ADAMS, N. & SAGAUT, P. 2013 *Large eddy simulation for compressible flows*. Springer.
- GERMANO, M. 1992 Turbulence: the filtering approach. *J. Fluid Mech.* **238**, 325–336.
- GOTO, S., SAITO, Y. & KAWAHARA, G. 2017 Hierarchy of antiparallel vortex tubes in spatially periodic turbulence at high Reynolds numbers. *Phys. Rev. Fluids* **2**, 064603.
- GOTTLIEB, S. & SHU, C.-W. 1998 Total variation diminishing Runge-Kutta schemes. *Math. Comput.* **67**, 73–85.
- HELLINGER, P., PAPINI, E., VERDINI, A., LANDI, S., FRANCI, L., MATTEINI, L. & MONTAGUD-CAMPS, V. 2021a Spectral transfer and Kármán–Howarth–Monin equations for compressible hall magnetohydrodynamics. *Astrophys. J.* **917**, 101.
- HELLINGER, P., VERDINI, A., LANDI, S., PAPINI, E., FRANCI, L. & MATTEINI, L. 2021b Scale dependence and cross-scale transfer of kinetic energy in compressible hydrodynamic turbulence at moderate Reynolds numbers. *Phys. Rev. Fluids* **6**, 044607.
- JAGANNATHAN, S. & DONZIS, D. A. 2016 Reynolds and Mach number scaling in solenoidally-forced compressible turbulence using high-resolution direct numerical simulations. *J. Fluid Mech.* **789**, 669–707.
- JOHNSON, P. L. 2020 Energy transfer from large to small scales in turbulence by multiscale nonlinear strain and vorticity interactions. *Phys. Rev. Lett.* **124**, 104501.
- JOHNSON, P. L. 2021 On the role of vorticity stretching and strain self-amplification in the turbulence energy cascade. *J. Fluid Mech.* **922**, A3.
- KIDA, S. & ORSZAG, S. A. 1992 Energy and spectral dynamics in decaying compressible turbulence. *J. Sci. Comput.* **7**, 1–34.
- KOLMOGOROV, A. N. 1941a Dissipation of energy in locally isotropic turbulence. *Dokl. Akad. Nauk SSSR* **32**, 16–18.
- KOLMOGOROV, A. N. 1941b The local structure of turbulence in incompressible viscous fluid for very large Reynolds numbers. *Dokl. Akad. Nauk SSSR* **30**, 299–303.
- KOVASZNAVY, L. S. 1953 Turbulence in supersonic flow. *J. Aeronaut. Sci.* **20**, 657–674.
- KRITSUK, A. G., WAGNER, R. & NORMAN, M. L. 2013 Energy cascade and scaling in supersonic isothermal turbulence. *J. Fluid Mech.* **729**, R1.
- LAI, C. C. K., CHARONKO, J. J. & PRESTRIDGE, K. 2018 A Kármán–Howarth–Monin equation for variable-density turbulence. *J. Fluid Mech.* **843**, 382–418.
- LELE, S. K. 1992 Compact finite difference schemes with spectral-like resolution. *J. Comput. Phys.* **103**, 16–42.
- LIN, C. C. 1947 Remarks on the spectrum of turbulence. In *Proceedings of the First Symposium of Applied Mathematics*.
- LINDBORG, E. 2019 A note on acoustic turbulence. *J. Fluid Mech.* **874**, R2.
- MCKEOWN, R., PUMIR, A., RUBINSTEIN, S. M., BRENNER, M. P. & OSTILLA-MÓNICO, R. 2023 Energy transfer and vortex structures: visualizing the incompressible turbulent energy cascade. *New J. Phys.* **25**, 103029.
- MENEVEAU, C. & KATZ, J. 2000 Scale-invariance and turbulence models for large-eddy simulation. *Annu. Rev. Fluid Mech.* **32**, 1–32.

- MIURA, H. & KIDA, S. 1995 Acoustic energy exchange in compressible turbulence. *Phys. Fluids* **7**, 1732.
- MODESTI, D., SATHYANARAYANA, S., SALVADORE, F. & BERNARDINI, M. 2022 Direct numerical simulation of supersonic turbulent flows over rough surfaces. *J. Fluid Mech.* **942**, A44.
- MONIN, A. S. & YAGLOM, A. M. 1975 *Statistical Fluid Mechanics*. Cambridge University Press.
- MOSER, R. D., HAERING, S. W. & YALLA, G. R. 2021 Statistical properties of subgrid-scale turbulence models. *Annu. Rev. Fluid Meth.* **53**, 255–286.
- OGDEN, D. E., GLATZMAIER, G. A. & WOHLLETZ, K. H. 2008 Effects of vent overpressure on buoyant eruption columns: implications for plume stability. *Earth Planet. Sci. Lett.* **268**, 283–292.
- PAN, S. & JOHNSEN, E. 2017 The role of bulk viscosity on the decay of compressible, homogeneous, isotropic turbulence. *J. Fluid Mech.* **833**, 717–744.
- PIROZZOLI, S. & GRASSO, F. 2004 Direct numerical simulations of isotropic compressible turbulence: Influence of compressibility on dynamics and structures. *Phys. Fluids* **16**, 4386–4407.
- POPE, S. B. 2000 *Turbulent flows*. Cambridge University Press.
- QI, H., LI, X., HU, R. & YU, C. 2022 Quasi-dynamic subgrid-scale kinetic energy equation model for large-eddy simulation of compressible flows. *J. Fluid Mech.* **947**, A22.
- QIAN, J. 1994 Skewness factor of turbulent velocity derivative. *Acta Mech. Sin.* **10**, 12–15.
- RICHARDSON, L. F. 1922 *Weather Prediction by Numerical Processes*. Cambridge: Cambridge University Press.
- SAGAUT, P. 1995 Simulations numériques d'écoulements décollés avec des modèles de sous-maille. PhD thesis, Paris 6.
- SAGAUT, P. 2006 *Large Eddy Simulation for Incompressible Flows (3rd edition)*. Springer.
- SAGAUT, P. & CAMBON, C. 2018 *Homogeneous Turbulence Dynamics*, 2nd edn. Springer Cham.
- SAMTANEY, R., PULLIN, D. I. & KOSOVIC, B. 2001 Direct numerical simulation of decaying compressible turbulence and shocklet statistics. *Phys. Fluids* **13**, 1415.
- SCALO, J. & ELMEGREEN, B. G. 2004 Interstellar turbulence II: implications and effects. *Annu. Rev. Astron. Astrophys.* **42**, 275–316.
- SCHMIDT, W. & GRETE, P. 2019 Kinetic and internal energy transfer in implicit large-eddy simulations of forced compressible turbulence. *Phys. Rev. E* **100**, 043116.
- SMAGORINSKY, J. 1963 General circulation experiments with the primitive equations. *Mon. Weather Rev.* **91**, 99–164.
- SPINA, E. F., SMITS, A. J. & ROBINSON, S. K. 1994 The physics of supersonic turbulent boundary layers. *Annu. Rev. Fluid Mech.* **26**, 287–319.
- TENNEKES, H. & LUMLEY, J. L. 1972 *A First Course in Turbulence*. MIT Press.
- VON KÁRMÁN, T. & HOWARTH, L. 1938 On the statistical theory of isotropic turbulence. *Proc. R. Soc. Lond. A* **164**, 192.
- VON KÁRMÁN, T. & LIN, C. C. 1951 On the statistical theory of isotropic turbulence. *Adv. Appl. Mech* **2**, 1.
- WAGNER, R., FALKOVICH, G., KRITSUK, A. G. & NORMAN, M. L. 2012 Flux correlations in supersonic isothermal turbulence. *J. Fluid Mech.* **713**, 482–490.
- WALTRUP, P. J. 1987 Liquid-fueled supersonic combustion ramjets—a research perspective. *J. Propuls. Power* **3**, 515–524.
- WANG, J., GOTOH, T. & WATANABE, T. 2017 Spectra and statistics in compressible isotropic turbulence. *Phys. Rev. Fluids* **2**, 013403.
- WANG, J., SHI, Y., WANG, L.-P., XIAO, Z., HE, X. T. & CHEN, S. 2012a Effect of compressibility on the small-scale structures in isotropic turbulence. *J. Fluid Mech.* **713**, 588–631.
- WANG, J., SHI, Y., WANG, L.-P., XIAO, Z., HE, X. T. & CHEN, S. 2012b Scaling and statistics in three-dimensional compressible turbulence. *Phys. Rev. Lett.* **108**, 214505.
- WANG, J., YANG, Y., SHI, Y., XIAO, Z., HE, X. T. & CHEN, S. 2013 Cascade of kinetic energy in three-dimensional compressible turbulence. *Phys. Rev. Lett.* **110**, 214505.
- YANG, P.-F., FANG, J., FANG, L., PUMIR, A. & XU, H. 2022 Low-order moments of the velocity gradient in homogeneous compressible turbulence. *J. Fluid Mech.* **947**, R1.
- YANG, P.-F., PUMIR, A. & XU, H. 2018 Generalized self-similar spectrum and the effect of large-scale in decaying homogeneous isotropic turbulence. *New J. Phys.* **20**, 103035.
- YANG, P.-F., ZHOU, Z., XU, H. & HE, G. 2023 Strain self-amplification is larger than vortex

stretching due to an invariant relation of filtered velocity gradients. *J. Fluid Mech.* **955**, A15.

YOSHIZAWA, A. 1986 Statistical theory for compressible turbulent shear flows, with the application to subgrid modeling. *Phys. Fluids* **29**, 2152–2164.

ZHANG, X., DHARIWAL, R., PORTWOOD, G., KOPS, S. M. D. & BRAGG, A. D. 2022 Analysis of scale-dependent kinetic and potential energy in sheared, stably stratified turbulence. *J. Fluid Mech.* **946**, A6.